Journal of Materials Chemistry A

PAPER

View Article Online
View Journal

Cite this: DOI: 10.1039/c6ta00454g

2D amorphous iron phosphate nanosheets with high rate capability and ultra-long cycle life for sodium ion batteries†

Tongchao Liu,[a] Yandong Duan,[a] Guangxing Zhang,[a] Maofan Li,[a] Yancong Feng,[a] Jiangtao Hu,[a] Jiaxin Zheng,[a] Jitao Chen[ab] and Feng Pan*[a]

Received 17th January 2016
Accepted 19th February 2016

DOI: 10.1039/c6ta00454g

www.rsc.org/MaterialsA

In our previous work, we reported the formation and mechanism of mono/bi-layer phosphate-based materials and their high performance as cathode materials for Li-ion batteries. In this work, we report that 2D amorphous nanosheets can be used as cathode materials to achieve outstanding performance for sodium ion batteries (SIBs) *e.g.* a high initial discharge capacity of 168.9 mA h g^{-1} at 0.1C, ultra-long life (92.3% capacity retention over 1000 cycles), and high rate capability (77 mA h g^{-1} at 10C) for Na-ion storage, whose electrochemical performance is also much superior to the reported amorphous $FePO_4$ or olivine $NaFePO_4$ with advantages of short paths and larger implantation surface areas for fast Na-ion diffusion and large specific surfaces with more interfacial capacitance. Interestingly, $NaFePO_4$ nano-crystals with about 10 nm sizes are self-nucleated from amorphous 2D nanosheets in the charge/discharge process, which was verified by transmission electron microscopy (TEM) and *in situ* electrochemical impedance spectroscopy (EIS).

Introduction

Lithium (Li)-ion batteries (LIBs) are the modern high-performance energy storage devices for portable electronics and increasingly for electrical vehicles due to their high energy and power densities.[2] However, with the increasingly serious energy crisis, the extensive application of LIBs faces important challenges related to both Li availability and cost.[3] Using sodium-ion batteries (SIBs) as an alternative attracted great interest, because Na is more abundant than Li and is easy to recover.[4] In addition, the intercalation chemistry of Na and Li is similar, thus the known LIB knowledge can be exploited in SIB.[5] Nevertheless, many challenges need to be overcome before SIBs can become commercially competitive with LIBs. For instance, compared with lithium, sodium weighs more and has a higher ionization potential and a larger ionic radius, which leads to a lower theoretical capacity and poor rate capacity.

Since the performance of SIBs (*e.g.* specific capacity and operating voltage) is largely dependent on the electrochemical properties of the electrode materials, it is of great importance to develop suitable electrode materials for SIBs.[6–8] Among them, phosphate-based materials have been identified as potential electroactive materials for SIBs,[9] such as $NaFePO_4$ (olivine),[10–13] $NaVPO_4F$,[14–16] $Na_3V_2(PO_4)_2F_3$,[17–19] $Na_{1.5}VOPO_4F_{0.5}$,[20,21] Na_2FePO_4F,[22] $Na_3V_2(PO_4)_3$,[23–26] $Na_3Al_2(PO_4)_2F_2$,[27,28] Na_2NiPO_4F,[29] $Na_2(Fe_{1-x}Co_x)PO_4F$,[30] $Na_2(Fe_{1-x}Mg_x)PO_4F$,[31] *etc.* However, crystalline phosphates have so far exhibited poor electrochemical performance for SIBs, because the undersized channel of the lattice limits the diffusion of Na ions. Thus, compared with LIBs, the crystalline phosphate-based sodium cathode materials show poor rate capability and cycling stability,[32,33] which limits the commercial development of SIBs.

In previous work,[1] we reported the formation of a special amorphous mono/bi-layer phosphate-based material and its performance as a cathode material for LIBs, with some natural advantages such as: shorter paths and larger implantation surface areas for fast Li-ion diffusion and large specific surface areas with more interfacial capacitance. When applied in LIBs, it shows excellent performance with high capacity and rate capability. In view of the above natural advantages, such 2D nanosheets should have excellent performance when applied in sodium ion batteries. Herein, we used previous methods to synthesize mono/bi-layer iron phosphate 2D nanosheets to be used as a novel cathode for SIBs, which show excellent performance: a high initial discharge capacity of 168.9 mA h g^{-1} at 0.1C, ultra-long life (92.3% capacity retention over 1000 cycles), and high rate capability (77 mA h g^{-1} at 10C) for Na-ion storage. Interestingly, $NaFePO_4$ nano-crystals are self-nucleated by electrochemical forces driven from the oxidation of amorphous 2D nanosheets during the charge/discharge process.

[a]School of Advanced Materials, Peking University, Peking University Shenzhen Graduate School, Shenzhen 518055, China. E-mail: panfeng@pkusz.edu.cn; Tel: +86-755-26033200

[b]Beijing National Laboratory for Molecular Sciences, College of Chemistry and Molecular Engineering, Peking University, Beijing 100871, China

† Electronic supplementary information (ESI) available: Experimental procedures, figures and tables. See DOI: 10.1039/c6ta00454g

Experimental

Materials

Atomically thin amorphous 2D-sheets are controllably prepared through a simple chemically induced precipitation method and post-processing, similar to our previous work.[1] The two main fabrication steps are the preparation of the precursor and post-processing by water and ethanol. For the preparation of the precursor, $FeSO_4 \cdot 7H_2O$, H_3PO_4, and $LiOH \cdot H_2O$ were used as the starting materials. Firstly, 1.05 g $FeSO_4 \cdot 7H_2O$ was dissolved in 33.30 g of ethylene glycol with nitrogen protection. Secondly, 0.55 g H_3PO_4 was mixed in 8.80 g of ethylene glycol and then the solution was slowly introduced into the $FeSO_4$ solution under stirring. Thirdly, 0.43 g LiOH was added into 41.6 g of ethylene glycol, dissolved under ultrasonic treatment and then the solution was added into the prior mixed solution, resulting in a dark green precursor. For the post-processing step, the precursor was washed twice with water and once with ethanol. Finally, the product was dried in a vacuum drying oven at 80 °C.

Material characterization

X-ray powder diffraction patterns were collected from a Bruker D8 Advance diffractometer with Cu Kα ($\lambda = 0.15418$ nm) at the 2θ range of 10–80° with a step of 0.02° and a testing time of 1 s. The morphologies were observed by using a SEM (ZEISS Supra 55) and a TEM (FEI Tecnai G2 F20 S-Twin). The energy-dispersive spectroscopy (EDS) was performed by using an Oxford-Max20 detector attached to the SEM. The thickness of nanosheets was measured by using an AFM (Bruker MultiMode 8).

Electrochemical measurements

Electrochemical characterization was performed with 2032 coin cells. For the cathode, $FePO_4$@C and PTFE (polytetrafluoroethylene) binder were mixed with isopropanol, in which the weight ratio was 80 : 20. By grinding in an agate mortar, $FePO_4$@C and the PTFE binder were mixed evenly, resulting in the cathode plate, and then dried in a vacuum at 110 °C for 12 h. Sodium metal anodes were prepared by cutting and planishing sodium pieces. The 2032 coin cells were assembled with the above cathode plates, sodium metal anodes and electrolytes. All the cells were assembled in a glove box tested at room temperature. The electrochemical characteristics of cells were determined on a NEWARE battery cycler in the voltage range of 1.4–3.8 V (*vs.* Na^+/Na). The cyclic voltammetry (CV) results were obtained by using a CHI 604E (Chenhua Instruments Co., China). The electrochemical impedance spectra were collected from 10^4 to 0.1 Hz and the amplitude was 10 mV.

Results and discussion

Fig. 1 shows the morphology of the as-prepared amorphous 2D nanosheets for this work characterized by TEM and AFM, and the schematics of the formed hybrid cathode materials $(Fe(II)_3(PO_4)_2 \cdot Fe(III)_3(PO_4)_2(OH)_3 \cdot nH_2O$/C ("FP@C")) by mixing the 2D nanosheets with carbon black by ball milling. The SEM and TEM images show large scale nanosheets prepared for this work with an average size of more than 1 μm (Fig. S1–S3† and Fig. 1a). High-resolution TEM images clearly illustrate no crystal lattice (Fig. 1b), and the Selected Area Electron Diffraction (SAED) images also show no signals of crystalline diffraction

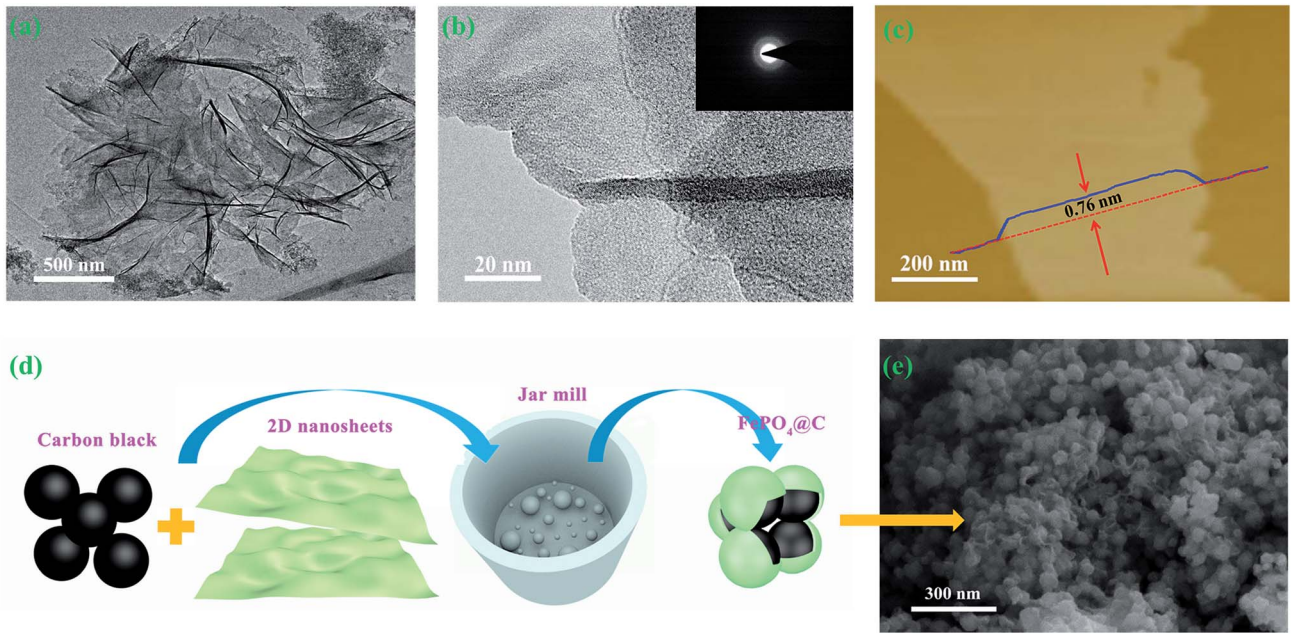

Fig. 1 (a) TEM image of 2D nanosheets (b) high-resolution TEM (HR-TEM) images of the 2D nanosheets. The inset is a selected area electron diffraction image of the 2D nanosheets. (c) AFM image of a typical nanosheet with a thickness of 0.74 nm, corresponding to one atomic layer. (d) The schematics of formed hybrid cathode materials $(Fe(II)_3(PO_4)_2 \cdot Fe(III)_3(PO_4)_2(OH)_3 \cdot nH_2O$/C ("FP@C")) by mixing the 2D nanosheets with carbon black by ball milling. (e) The SEM images of the mixture of nanosheets and carbon black.

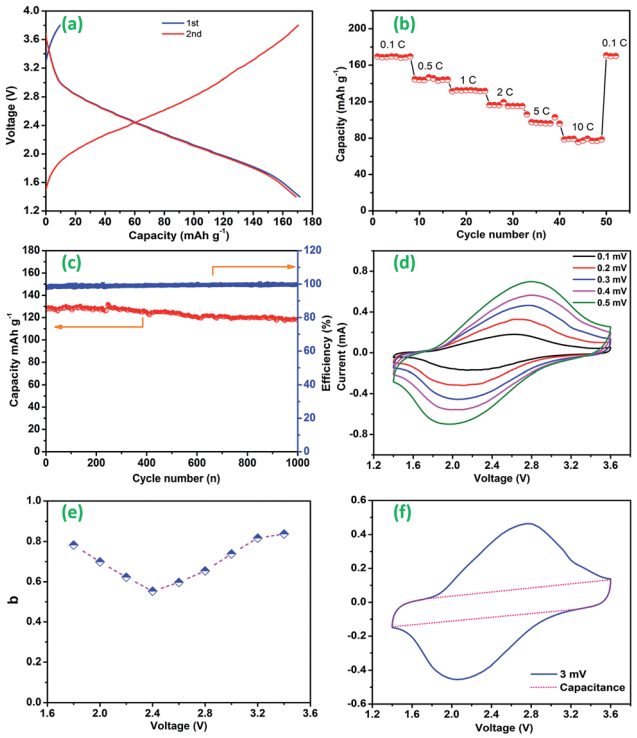

Fig. 2 (a) Galvanostatic discharging/charging profiles obtained at 0.1C. (b) Capacity *versus* cycle number at 0.1C, 0.5C, 1C, 2C, 5C, 10C and return to 0.1C. (c) Cycling performance of the sodium ion battery of 2D nanosheets. The capacity retention at 1C is about 92.3%, declining from 127.8 mA h g^{-1} at the first cycle to 117.9 mA h g^{-1} at the 1000th cycle. (d) CV curves conducted at scan rates of 0.1 mV s^{-1} to 0.5 mV s^{-1}. (e) The *b*-values of the different voltages. (f) CV curves and the capacitance contribution.

spots, indicating the amorphous structure of the prepared 2D nanosheets, which was further indicated by X-ray Diffraction (XRD), as shown in Fig. S5.† The thicknesses of the thin films measured by AFM are 0.76 nm and 1.55 nm, as shown in Fig. 1c and S4.† In order to make full use of 2D nanosheets' natural advantages, we created a special 2D nanosheet coated carbon black structure, where the 2D nanosheets were triturated and evenly coated on the surface of carbon black by ball milling (Fig. 1d). Therefore, 2D nanosheets have close contact with carbon black, and carbon black forms an excellent conductive network. After the ball milling process, the 2D nanosheets still retained the amorphous structure, indicated by XRD (Fig. S5†). The SEM images and EDS mapping show that the 2D nanosheets and carbon black had been fully mixed together as "FP@C" (Fig. 1e and S6†).

To demonstrate the advantages of these 2D nanosheets, we evaluated their performance as cathode materials for SIBs, in which the sodium metal was used as the counter electrode and 1 M $NaClO_4$ dissolved in a mixture of EC and DMC was used as the electrolyte.[34] Fig. 2a shows the charge/discharge curves of the 2D nanosheet hybrid cathode within a cut-off voltage window of 1.4–3.8 V *versus* Na^+/Na at a current rate of 0.1C (1C = 170 mA g^{-1}). The first discharge capacity is very high, about 168.9 mA h g^{-1}. Note that because of the absence of sodium ions, Fe(II) in FP@C is oxidized to Fe(III) in the first charge with a capacity of about 9.5 mA h g^{-1}. After the second charge/discharge cycle, the electrode delivers normal charge and discharge curves. These 2D nanosheets also show excellent rate capability at charge/discharge current rates ranging from 0.1–10C, as shown in Fig. 2b. The average capacities are 168, 145, 132, 116, 96, and 77 mA h g^{-1} at charge/discharge current rates of 0.1, 0.5, 1, 2, 5 and 10C, respectively. After high-rate charge/discharge cycling, a specific capacity of 170.1 mA h g^{-1} is restored when the current density is back to 0.1C. All these results indicate that 2D nanosheets exhibit an excellent rate capability and electrochemical reversibility for sodium ion storage. To the best of our knowledge, this excellent rate capability is reported for the first time in types of olivine $NaFePO_4$ and amorphous $FePO_4$. The cycling performance of the 2D nanosheets was measured at a current density of 1C, as shown in Fig. 2c. After 1000 cycles, the capacity declines slightly from 127.8 to 117.9 mA h g^{-1}, by a factor of 7.7%, which is superior to those reported types of $NaFePO_4$ materials. The cyclic voltammogram (CV) curve shows a pair of current peaks positioned at 2.6 and 2.2 V (Fig. 2d), corresponding to the deintercalation/intercalation of sodium ions, respectively. The broad deintercalation peaks imply a continuous single-phase de-intercalation reaction, which is quite different from that of the olivine $NaFePO_4$ characterized by a biphasic transition during the sodium ion de-intercalation/intercalation.

Table 1 shows a comparison of our work with the reported studies on SIBs based on amorphous $FePO_4$ or olivine $NaFePO_4$ with high performance. Hu[35] reported that porous amorphous

Table 1 The comparison of our work with the reported studies on SIBs based on amorphous $FePO_4$ or olivine $NaFePO_4$

Compound	Capacity (mA h g^{-1})	Rate capacity (mA h g^{-1})	Cycling performance
Our paper	169 (0.1C)	77 (10C)	92.3% (1000 cycle 1C)
Amorphous-$FePO_4$ (ref. 35)	120 (0.1C)	50 (1C)	98% (40 cycle 0.5C)
Amorphous-$FePO_4$ (ref. 36)	151 (0.1C)	44 (10C)	94% (160 cycle 0.1C)
Amorphous-$FePO_4$ (ref. 37)	142 (0.1C)	64 (1C)	92% (120 cycle 0.1C)
Amorphous-$FePO_4$ (ref. 38)	155 (0.1C)	75 (1C)	—
Maricite-$NaFePO_4$ (ref. 12)	142 (0.05C)	66 (2C)	95% (200 cycle 0.1C)
Olivine-$NaFePO_4$ (ref. 33)	111 (0.1C)	46 (2C)	90% (240 cycle 0.1C)
Olivine-$NaFePO_4$ (ref. 39)	120 (0.05C)	25 (2C)	90% (100 cycle 0.1C)
Olivine-$NaFePO_4$ (ref. 11)	125 (0.05C)	85 (0.5C)	90% (50 cycle 0.1C)

$FePO_4$ nanoparticles mixed with single-wall carbon nanotubes showed cell performance for Na-ion storage. The electrochemical performance shows that the discharge capacity is 120 mA h g^{-1} at 0.1C rate (10 mA g^{-1}), and the capacity still remains at 50 mA h g^{-1} after 300 cycles at 1C rate (100 mA g^{-1}). Cao[36] reported that amorphous $FePO_4$ nanospheres showed high-performance for sodium ion batteries with a high initial discharging capacity of 151 mA h g^{-1} at 20 mA g^{-1}, good cycle stability (94% capacity retention ratio over 160 cycles), as well as high rate capability (44 mA h g^{-1} at 1000 mA g^{-1}). Xu[37] reported that amorphous $FePO_4$ nanoparticles showed an initial specific-discharge capacity of 142 mA h g^{-1}, reversible capacity of 130.8 mA h g^{-1} after 120 cycles, and high rate capability of 63.5 mA h g^{-1} at 1C. Liu[38] reported that $FePO_4$@MCNT nanowire showed excellent cell performance with a discharge specific capacity of 155.2 mA h g^{-1} in the initial cycle and 157.2 mA h g^{-1} after 70 cycles at 0.1C. From Table 1, we can see that our 2D nanosheets show the best electrochemical performance among all reported.

The reasons for the 2D nanosheets to show the remarkable electrochemical performance with high capacity, high rate capacity, and long life can be attributed to the factors given below. Compared with amorphous $FePO_4$ and olivine $NaFePO_4$, the 2D nanosheets create shorter paths and larger implantation surface areas for fast Li/Na-ion diffusion. The energy barrier of Na ion insertion of 2D-Na is much lower than that in bulks of olivine $NaFePO_4$. Because of the larger ionic radius, Na ions are difficult to insert into undersized channels of bulks of olivine $NaFePO_4$. For 2D nanosheets, the diffusion of sodium ions is not limited in mono/bi-layer materials. Another reason is that the large surfaces of the 2D nanosheets would contribute large interfacial capacitance to the total capacity. Similar to 2D nanosheets in lithium ion batteries, to investigate the effect of the capacitance-type behavior of 2D nanosheets on their electrochemical performance, we measured a series of CV curves at scan rates of 0.1–0.5 mV s^{-1}. The shapes of these CV curves (Fig. 2d) show no distortion with the speeding up of the scanning rate, meaning that the 2D nanosheets exhibit an excellent rate capability. Assuming that the current and the scan rate follow a power-law relationship,[40] $I_p = av^b$, where a and b are adjustable values. The b value of 0.5 indicates that the current is controlled by semi-infinite linear diffusion, while the b value of 1 indicates that the current is surface-controlled like capacitance.[41] The b-values obtained in the range of 1.8–3.6 V are between 0.503 and 0.838, indicating a concurrence of both sodium ion semi-infinite linear diffusion and surface-controlled pseudocapacitance (Fig. 2e). We further investigated the capacitance contribution to the sodium ion battery capacity, as shown in Fig. 2f. According to CV curves, the electric quantity of the whole cycle and the capacitance part were calculated separately by numerical integration. The results show that the capacitive contribution in the sodium ion battery is almost unchanged at any scan rate, and interfacial capacitance accounted for 31.7–33.8% of the total capacity, as shown in Fig. S7.†

We further compared the electrochemical performance of 2D nanosheet SIBs (2D-Na) with that of 2D nanosheet LIBs (2D-Li). As shown in Fig. 3a, the average voltage of the discharge curve of

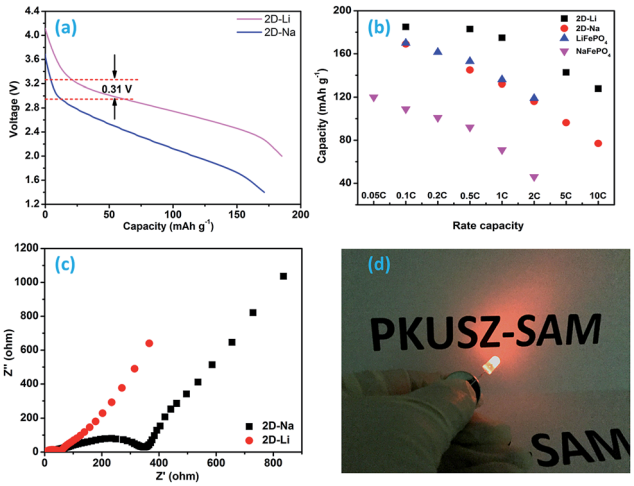

Fig. 3 (a) Discharge curve of 2D-Na and 2D-Li. (b) Rate capability of 2D-Li, 2D-Na, $LiFePO_4$ and $NaFePO_4$. (c) Electrochemical impedance spectroscopy (EIS) of 2D-Li and 2D-Na. (d) The image of an LED lit by a 2D nanosheet sodium ion battery.

2D-Na is lower than that of 2D-Li by 0.31 V, which is smaller than the voltage reduction of 0.53 V from olivine $LiFePO_4$ to $NaFePO_4$.[42] In addition, compared with bulk crystalline materials, the variation of the rate capability between 2D-Li and 2D-Na is much smaller (Fig. 3b). For example, the capacity of bulk olivine $NaFePO_4$ is decreased from 120 mA h g^{-1} @ 0.1C to 40 mA h g^{-1} @ 2C, 2.5 times larger than the capacity decrease for olivine $LiFePO_4$ (168 mA h g^{-1} @ 0.1C *vs.* 120 mA h g^{-1} @ 2C). In contrast, the capacity of 2D-Na is decreased from 169 mA h g^{-1} @ 0.1C to 77 mA h g^{-1} @ 10C, 1.5 times larger than the capacity decrease for 2D-Li (185 mA h g^{-1} @ 0.1C and 127 mA h g^{-1} @ 10C for 2D-Li). The much better rate capability performance of 2D-Na is due to the absence of undersized channels for diffusion. We further compared the resistance of 2D-Li and 2D-Na (Fig. 3c), and the data are analyzed according to the following equation:[43]

$$D_{Li^+} = R^2T^2/2A^2n^4F^4C^2\kappa^2$$

where R is the gas constant, T is the absolute temperature, A is the surface area of the electrode, n is the number of electrons per molecule, F is the Faraday constant, C is the concentration of Li-ions, and κ is the Warburg factor to be determined from the slope of the low frequency part of resistance. It can be seen that 2D-Li and 2D-Na have a similar κ, so the diffusion coefficients of those are similar, which further indicates 2D nanosheets with shorter diffusion paths for cation storage.

Electrochemical impedance spectroscopy (EIS) is used to study the electrode reaction kinetics of 2D-Na. We tested the EIS of the coin cell after 1, 10, 20, 40, and 100 cycles at 1C as shown in Fig. 4a and Fig. S8,† in which the visible semicircles in the high and middle frequency ranges reflect the solid-electrolyte interface (SEI) resistance (R_{SEI}) and charge transfer resistance (R_{ct}), respectively. Similar to ref. 1, the third semicircle appears in the low frequency ranges with charge/discharge cycles, which indicates that additional diffusion behavior appears in semi-

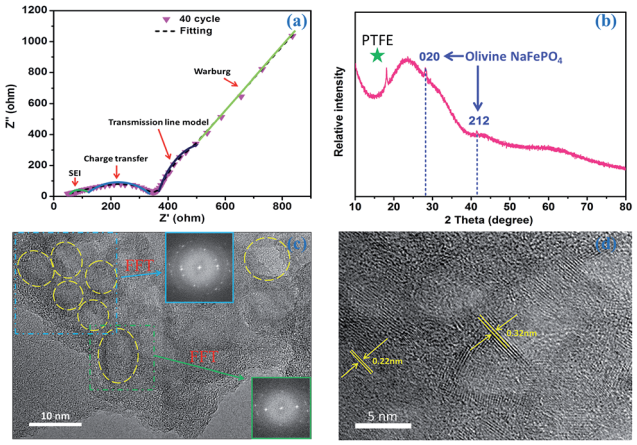

Fig. 4 (a) Electrochemical impedance spectroscopy (EIS) and the fitting curve for 40 charge/discharge cycles. (b) XRD pattern for crystallization of nanosheets after 1000 cycles. (c) TEM image for crystallization of 2D nanosheets. The inset is the FFT figure of 2D nanosheets. (d) HR-TEM image for crystallization of 2D nanosheets.

infinite linear diffusion. We speculate that the additional diffusion behavior is associated with the formation of $NaFePO_4$ nano-crystalline particles as the new "second-phase" (see Fig. 4c and d). The "transmission line" model is proposed to explain the special EIS features. Due to the presence of amorphous and crystal phases in the 2D nanosheets, the Na^+ can diffuse into/from the amorphous phase and $NaFePO_4$ nano-crystalline particles during the discharge/charge process, which leads to two kinds of diffusion behavior and the second semicircle.

To further validate the second phase generated after cycling, we dismantled the coin cell after 1000 cycles at 1C and cleaned the electrode materials for EDS, XRD and TEM analyses. The EDS mapping (Fig. S9†) shows Na ion insertion into the 2D nanosheets. Fig. 4b shows the XRD patterns of the electrode materials with strong reflection peaks at 28.2 and 41.4, which correspond to the phase structure of (020) and (212) planes of crystalline $NaFePO_4$, respectively. The TEM (Fig. S10† and Fig. 4c) images show that the morphology of 2D nanosheets remains unchanged and many nano-crystal particles with 10–15 nm sizes are inside the 2D nanosheets. Furthermore, the high magnification TEM images (Fig. 4d and Fig. S11†) revealed the obvious lattice channels in the nano-particles with two interplanar distances of about 0.22 nm and 0.32 nm. This finding is consistent with the d_{212} value (0.22 nm) and the d_{020} value (0.32 nm), calculated from the XRD pattern of olivine $NaFePO_4$ crystals. Thus, both TEM and XRD results strongly proves that olivine $NaFePO_4$ nano-crystals can be nucleated and grown from atomically thin amorphous 2D nanosheets in the electrochemical charge/discharge cycles. The nucleation of $NaFePO_4$ nano-crystals (limited sizes about 10–15 nm) from amorphous matrix is interesting. Its mechanism can be proposed that $NaFePO_4$-like short-ordering structures in the amorphous 2D nanosheets can become nucleation-centers, but it is hard to grow a nucleus of big size because of the high mobility resistance of the iron phosphate group in the solid amorphous phase. The ratio of $NaFePO_4$ nano-crystalline part to amorphous part is difficult to be defined.

Conclusions

We used the synthesized mono/bi-layer amorphous iron phosphate nanosheets milled with carbon black to generate hybrid cathode materials for SIBs, which show a high reversible capacity of 168.9 mA h g^{-1} @ 0.1C, high rate capability of 77 mA h g^{-1} @ 10C, and an excellent cycling stability with 92.3% capacity retention after 1000 cycles. This electrochemical performance is also superior to the reported high performance of SIBs based on amorphous $FePO_4$ or olivine $NaFePO_4$. The high performance can be attributed to the shorter paths and larger implantation surface areas for fast Na-ion diffusion and more interfacial capacitance in such mono/bi-layer amorphous iron phosphate nanosheets. Interestingly, self-nucleated $NaFePO_4$ nano-crystals with sizes of about 10–15 nm as the new phase can be *in situ* observed by EIS during the electrochemical charge/discharge cycles. This work reveals that the atomically thin 2D nanosheets can become novel electrode materials with the hybrid behavior of batteries and supercapacitors for high-performance sodium ion batteries.

Acknowledgements

The research was financially supported by Guangdong Innovation Team Project (No. 2013N080) and Shenzhen Science and Technology Research Grant (peacock plan KYPT20141016105435850).

References

1 T. Liu, Y. Feng, Y. Duan, S. Cui, L. Lin, J. Hu, H. Guo, Z. Zhuo, J. Zheng and Y. Lin, *Nano Energy*, 2015, **18**, 187–195.
2 J. M. Tarascon and M. Armand, *Nature*, 2001, **414**, 359–367.
3 H. L. Pan, Y. S. Hu and L. Q. Chen, *Energy Environ. Sci.*, 2013, **6**, 2338–2360.
4 V. Palomares, P. Serras, I. Villaluenga, K. B. Hueso, J. Carretero-González and T. Rojo, *Energy Environ. Sci.*, 2012, **5**, 5884–5901.
5 M. S. Islam and C. A. J. Fisher, *Chem. Soc. Rev.*, 2014, **45**, 185–204.
6 Y. Naoaki, K. Kei, D. Mouad and K. Shinichi, *Chem. Rev.*, 2014, **114**, 11636–11682.
7 C. M. L. Croguennec, *Chem. Rev.*, 2013, **113**, 6552–6591.
8 K. Haegyeom, H. Jihyun, P. Kyu-Young, K. Hyungsub, K. Sung-Wook and K. Kisuk, *Chem. Rev.*, 2014, **114**, 11788–11827.
9 J. Lu, S. C. Chung, S. I. Nishimura and A. Yamada, *Chem. Mater.*, 2013, **25**, 3480–3487.
10 P. Moreau, D. Guyomard, J. Gaubicher and F. Boucher, *Chem. Mater.*, 2010, **22**, 4126–4128.
11 S. M. Oh, S. T. Myung, J. Hassoun, B. Scrosati and Y. K. Sun, *Electrochem. Commun.*, 2012, **22**, 149–152.
12 J. Kim, D. H. Seo, H. Kim, I. Park, J. K. Yoo, S. K. Jung, Y. U. Park, W. A. G. Iii and K. Kang, *Energy Environ. Sci.*, 2015, **8**, 540–545.

13 M. Casas-Cabanas, V. V. Roddatis, D. Saurel, P. Kubiak, J. Carretero-González, V. Palomares, P. Serras and T. Rojo, *J. Mater. Chem.*, 2012, **22**, 17421–17423.
14 J. Zhao, J. He, X. Ding, J. Zhou, Y. O. Ma, S. Wu and R. Huang, *J. Power Sources*, 2010, **195**, 6854–6859.
15 Y. Lu, S. Zhang, Y. Li, L. Xue, G. Xu and X. Zhang, *J. Power Sources*, 2014, **247**, 770–777.
16 M. W. Xu, C. Cheng, Q. Q. Sun, S. J. Bao, Y. B. Niu, H. He, Y. Li and J. Song, *RSC Adv.*, 2015, **5**, 40065–40069.
17 C. Zhu, K. Song, P. A. van Aken, J. Maier and Y. Yu, *Nano Lett.*, 2014, **14**, 2175–2180.
18 M. Bianchini, N. Brisset, F. Fauth, F. Weill, E. Elkaim, E. Suard, C. Masquelier and L. Croguennec, *Chem. Mater.*, 2014, **26**, 4238–4247.
19 Z. Liu, Y.-Y. Hu, M. T. Dunstan, H. Huo, X. Hao, H. Zou, G. Zhong, Y. Yang and C. P. Grey, *Chem. Mater.*, 2014, **26**, 2513–2521.
20 A. A. Tsirlin, R. Nath, A. M. Abakumov, Y. Furukawa, D. C. Johnston, M. Hemmida, H. A. K. V. Nidda, A. Loidl, C. Geibel and H. Rosner, *Phys. Rev. B: Condens. Matter Mater. Phys.*, 2011, **84**, 014429.
21 F. Sauvage, E. Quarez, J. M. Tarascon and E. Baudrin, *Solid State Sci.*, 2006, **8**, 1215–1221.
22 M. Ramzan, S. Lebègue, P. Larsson and R. Ahuja, *J. Appl. Phys.*, 2009, **106**, 043510–043516.
23 J. Gopalakrishnan and K. K. Rangan, *Chem. Mater.*, 1992, **4**, 745–747.
24 K. Saravanan, C. W. Mason, A. Rudola, K. H. Wong and P. Balaya, *Adv. Energy Mater.*, 2013, **3**, 444–450.
25 Z. Jian, W. Han, X. Lu, H. Yang, Y. S. Hu, J. Zhou, Z. Zhou, J. Li, W. Chen and D. Chen, *Adv. Energy Mater.*, 2013, **3**, 138.
26 S. Li, Y. Dong, L. Xu, X. Xu, L. He and L. Mai, *Adv. Mater.*, 2014, **26**, 3545–3553.
27 J.-M. Le Meins, M.-P. Crosnier-Lopez, A. Hemon-Ribaud and G. Courbion, *J. Solid State Chem.*, 1999, **148**, 260–277.
28 J.-M. Le Meins, O. Bohnke and G. Courbion, *Solid State Ionics*, 1998, **111**, 67–75.
29 B. L. Ellis, W. M. Makahnouk, W. Rowan-Weetaluktuk, D. Ryan and L. F. Nazar, *Chem. Mater.*, 2009, **22**, 1059–1070.
30 B. Prabeer, C. Jean-NoëL, R. Nadir, D. Charles, A. Mohamed, D. Loic, A. Michel and T. Jean-Marie, *ChemInform*, 2010, **49**, 7401–7413.
31 M. Avdeev, C. D. Ling, T. T. Tan, S. Li, G. Oyama, A. Yamada and P. Barpanda, *Inorg. Chem.*, 2013, **53**, 682–684.
32 A. Sun, F. R. Beck, D. Haynes, J. A. Poston, S. Narayanan, P. N. Kumta and A. Manivannan, *Mater. Sci. Eng., B*, 2012, **177**, 1729–1733.
33 Y. Fang, Q. Liu, L. Xiao, X. Ai, H. Yang and Y. Cao, *ACS Appl. Mater. Interfaces*, 2015, **7**, 17977–17984.
34 A. Ponrouch, E. Marchante, M. Courty, J. M. Tarascon and M. R. Palacín, *Energy Environ. Sci.*, 2012, **5**, 8572–8583.
35 Y. Liu, Y. Xu, X. Han, C. Pellegrinelli, Y. Zhu, H. Zhu, J. Wan, A. C. Chung, O. Vaaland, C. Wang and L. Hu, *Nano Lett.*, 2012, **12**, 5664–5668.
36 Y. Fang, L. Xiao, J. Qian, X. Ai, H. Yang and Y. Cao, *Nano Lett.*, 2014, **14**, 3539–3543.
37 Y. Liu, Y. Zhou, J. Zhang, S. Zhang and S. Xu, *Phys. Chem. Chem. Phys.*, 2015, **17**, 22144–22151.
38 S. Xu, S. Zhang, J. Zhang, T. Tan and Y. Liu, *J. Mater. Chem. A*, 2014, **2**, 7221–7228.
39 Y. Zhu, Y. Xu, Y. Liu, C. Luo and C. Wang, *Nanoscale*, 2013, **5**, 780–787.
40 J. Come, P. L. Taberna, S. Hamelet, C. Masquelier and P. Simon, *J. Electrochem. Soc.*, 2011, **158**, A1090–A1093.
41 A. Veronica, C. Jérémy, M. A. Lowe, K. Jong Woung, T. Pierre-Louis, S. H. Tolbert, H. D. Abruna, S. Patrice and D. Bruce, *Nat. Mater.*, 2013, **12**, 518–522.
42 S. P. Ong, V. L. Chevrier, G. Hautier, A. Jain, C. Moore, S. Kim, X. Ma and G. Ceder, *Energy Environ. Sci.*, 2011, **4**, 3680–3688.
43 C. Xuan, *J. Electrochem. Soc.*, 2013, **160**, A3048–A3053.

